JTSES
Journal of Thermal and Sustainable Energy Systems

https://jtses.com/index.php/home/index

Thermal and Optical Engineering of Semi-Transparent Photovoltaics for Vehicle Roof Integration under Real-World Driving Conditions

Elangovan Murugesan

Department of Mechanical Engineering, Sri Manakula Vinayagar Engineering College, Madagadipet, Puducherry 605107, India

* Corresponding Email: elangovan.mech@smvec.ac.in

Abstract

Vehicle-integrated photovoltaics (VIPV) have emerged as a promising approach to enhancing energy autonomy in electric vehicles by harnessing available roof surfaces to generate solar energy. However, dynamic factors such as varying incidence angles, shading, temperature fluctuations, and vibration during driving limit energy capture and are not accounted for in static laboratory tests. This study addressed the lack of comparative, on-road, technology-spanning analysis of semi-transparent thin-film photovoltaic absorbers under real automotive conditions. The objective was to evaluate and compare perovskite, CIGS, hydrogenated amorphous silicon, and organic photovoltaics using a combined optical–thermal–mechanical framework. Modules were integrated on a vehicle and tested through drive cycles representing highway, urban, and mixed routes, supported by synchronized telemetry, spectral filtering, goniometric angular analysis, and thermal/vibration stress protocols. Results showed that CIGS produced the highest areal energy output under highway conditions, while OPV led in mass-normalized yield due to its ultralight construction. Perovskite and OPV retained more output at oblique angles than CIGS, and perovskite demonstrated the lowest thermal degradation rate. Shading penalties varied significantly with interconnect geometry, and increasing perovskite segmentation reduced energy loss by 35%. Reinforcement learning–based MPPT improved tracking efficiency by up to 6 percentage points over traditional methods. These findings highlighted the influence of absorber selection, interconnect design, and controller choice on real-world energy yield. The research provided a foundation for engineering decisions in VIPV systems and emphasized the value of co-optimizing material properties with vehicle-specific integration constraints. Future studies could extend this framework to long-term fleet telemetry and predictive maintenance modeling.

Keywords: energy efficiency, renewable energy, vehicle-integrated photovoltaics, thermal engineering, maximum power point tracking

1. Introduction

Solar energy harvesting on vehicle surfaces is receiving growing attention because the electrification of transport increases the value of distributed, onboard power generation for auxiliary loads, battery support, and range extension. Vehicle roofs are especially attractive because they provide an exposed surface that can host lightweight photovoltaic laminates without competing directly with passenger or cargo space [17]. Vehicle-integrated photovoltaics, therefore, sit at the intersection of renewable energy engineering, automotive design, and advanced materials science, where optical efficiency, mechanical compliance, thermal stability, and electrical control must be considered together rather than in isolation. Semi-transparent thin-film technologies are particularly relevant in this setting because they can combine reduced mass, geometric adaptability, and controlled visible transmittance with the possibility of integration on curved glazing surfaces [1].

Photovoltaic performance is governed not only by nameplate conversion efficiency but also by the spectral, angular, thermal, and electrical conditions encountered during operation. In stationary installations, these influences are often accounted for through standardized laboratory procedures that enable fair comparisons across devices and laboratories. A vehicle roof, by comparison, is exposed to rapidly varying irradiance, repeated angular shifts caused by heading and body motion, intermittent shading from urban infrastructure, high module temperatures driven by solar loading, and continuous vibration originating from road excitation [16]. Automotive glazing further modifies the incident spectrum by attenuating ultraviolet and part of the visible range before light reaches the absorber, and roof curvature can introduce local strain and optical mismatch across the laminate. These

Received on 2026-03-26 Accepted on 2026-05-07

conditions make vehicle operation fundamentally different from flat, static photovoltaic deployment and create a strong need for testing strategies that reflect the coupled optical, thermal, mechanical, and control-system environment of a moving platform [2].

Thin-film photovoltaic absorbers offer distinct advantages and limitations for vehicle integration. CIGS modules have been valued for strong conversion efficiency in flexible formats and for monolithic interconnection schemes that suit elongated roof geometries [22]. Hydrogenated amorphous silicon has been used extensively in large-area deposition and has shown comparatively stable behavior after the initial light-induced drop associated with the Staebler–Wronski effect. Organic photovoltaics have attracted interest because their ultralow areal mass and mechanical compliance suit curved and weight-sensitive structures [21]. Semi-transparent perovskite devices have emerged as promising candidates because bandgap tuning, thin absorber layers, and low-temperature processing support a balance among optical transmission, electrical output, and aesthetic integration. Earlier studies described these technologies primarily through separate device-specific investigations, often under laboratory illumination and simplified mounting conditions. As a result, the practical choice among candidate absorbers for vehicle roofs remained uncertain, particularly when performance metrics were influenced by glazing-filtered spectra, elevated temperatures, fast irradiance ramps, and localized occlusions [3].

Previous research also examined components of the broader system supporting photovoltaic integration, including monitoring architectures, thermal management strategies, predictive control methods, and data-driven diagnostics. These studies improved the understanding of real-time sensing, algorithmic optimization, and maintenance planning in broader photovoltaic and energy-management applications [18]. Yet most of that work did not provide a controlled comparison among semi-transparent absorber families on a common vehicle platform. Many reports treated a single technology, a single driving or climate context, or a laboratory-only setting, which limited the ability to attribute performance differences to absorber physics, interconnect architecture, or control strategy [20]. Earlier shading studies often focused on fixed arrays or conventional modules rather than on narrow, roof-conformal laminates with distributed bypass elements. Prior MPPT research often relied on quasi-static current–voltage characteristics and assumed relatively slow irradiance variation, even though mobile operation subjected the roof to short-duration fluctuations caused by trees, buildings, roof appendages, and vehicle motion. Reliability investigations also tended to apply standard damp-heat and thermal-cycling protocols without linking those outcomes to actual energy yield under route-dependent conditions [14].

Table 1: Photovoltaic Performance, Integration, and Sustainability

Reference / Citation	**Objective / Aim**	**Methodology / Approach**	**Materials / Parameters Studied**	**Key Findings / Results**	**Relevance to Current Study**
Alombah et al., 2025	Develop and validate an IoT-based monitoring system for real-time PV evaluation	Design, prototyping, and experimental validation on a 30 W PV system	Irradiance, panel and ambient temperature, humidity, PV current and voltage	High adaptability (≤90 kW), reliable in harsh conditions, remote monitoring enabled, ↓ monitoring cost	Provides a robust monitoring platform; aligns with this study's need for synchronized telemetry [4]
Arun et al., 2024	Integrate PV into buildings using deep learning for energy management	Enhanced LSTM-based predictive microgrid control	PV–battery microgrid, home energy demand patterns	↑ prediction accuracy, ↑ efficiency, ↑ cost savings, ↓ reliance on non-renewables	Demonstrates the value of advanced control algorithms, informing MPPT and forecasting elements in this study[5]

Received on 2026-03-26 Accepted on 2026-05-07

Geetha, 2025	Reduce EV charging load on grid with PV-fed microgrid	Hybrid Skill Optimization Algorithm + Dilated Residual Network, exergy analysis	EV charging station with PV	Energy efficiency 96.2%, exergy efficiency 93.8%, outperforming PSO, BCO, WHO	Relates to vehicle-integrated PV use cases and validates hybrid optimization strategies[6]
Harrison et al., 2025	Provide a low-cost, realistic PV control verification platform	Real-Climatic Microcontroller-in-the-Loop (RCMIL)	MPPT controllers tested under real climate emulation	RCE = 97.15%, voltage MAE = 4.55 V, MAPE = 18.77%	Relevant to validating MPPT algorithms used in this research [7]
Jose et al., 2023	Enhance PV cooling with nanofluid-based serpentine heat exchangers	Experimental and CFD simulations	PV/T with water, Al2O3 nanofluids (0.1%, 0.2%)	↑ thermal efficiency (53.61% water → 71.02% with Al2O3 0.2%), ↑ exergy efficiency (20–36%)	Highlights temperature control relevance; supports analysis of thermal coefficients in this study [8]
Kalimuthukumar et al., 2022	Propose partial resonant inverter with sliding-mode MPPT for EV battery charging	Simulation and experimental prototype validation	PRI + doubler rectifier system	↑ efficiency, ↑ power quality, ↓ cost, ↓ size	Provides context for circuit-level MPPT innovations, complementary to system-level control focus here [9]
Panda et al., 2025	Optimize PV–battery systems with demand response in smart grids	MATLAB simulation, PSO vs LP optimization	Grid-connected PV–BESS microgrid, DR strategies	↑ cost savings (15.32%), ↑ stability, ↓ grid fluctuations	Relates to PV energy management strategies transferable to vehicle-integrated PV [10]
S et al., 2024	Detect PV module faults using machine learning	CNN feature extraction, J48 decision tree, Bayes classifiers	Delamination, glass breakage, discoloration, burn marks, snail trails	High accuracy in visual fault detection, ↑ reliability in maintenance	Connects to durability evaluation; supports focus on degradation under stress testing [11]
Singla et al., 2025	Improve PV cell modeling via multi-objective optimization	Parameter estimation algorithm vs traditional methods	PV cell models, empirical datasets	↑ accuracy, ↑ robustness, ↓ premature convergence	Provides modeling precision for simulating PV performance in this study [12]
Yadav et al., 2025	Assess PV waste recovery challenges in India	PCA + AHP multi-criteria analysis	Eight key challenges in PV waste	Hazardous recycling (83.2%), low recycling	Informs long-term sustainability considerations for PV deployment

Received on 2026-03-26 Accepted on 2026-05-07

	potential (83.4%), lack of technology as key barriers	examined here [13]

Across these studies (Table 1), a strong emphasis is placed on intelligent monitoring (IoT), advanced control (LSTM, optimization algorithms), and system reliability under real-world conditions. Research trends indicate significant gains in energy efficiency (up to 20%), exergy efficiency (up to 93.8%), and cost reductions (15% through optimization). Cooling strategies with nanofluids consistently improve PV performance (↑ thermal efficiency to 71%), while machine learning supports predictive fault detection, enhancing reliability. Sustainability concerns are increasingly addressed, with waste management challenges identified as critical future barriers. Collectively, these works highlight the convergence of real-time monitoring, intelligent control, durability engineering, and lifecycle sustainability as essential dimensions of modern PV integration.

These limitations left several unresolved questions in engineering design. It remained unclear which semi-transparent thin-film technology provides the best balance between areal and mass-normalized yields once modules are mounted on a real vehicle roof. The angular response of different absorber stacks under glazing-filtered light was not often measured in a consistent framework that allowed direct comparison across technologies [15]. Temperature coefficients and transient electrical behavior were seldom evaluated together with roof-level telemetry, even though thermal derating and rapid irradiance changes strongly affect power generation during driving [23]. The role of substring geometry and bypass-diode placement in mitigating localized shading on vehicle roofs also required clearer experimental evidence, particularly for emerging perovskite layouts. In addition, the value of advanced tracking algorithms under rapidly changing mobile conditions had not been quantified on identical electrical hardware and synchronized time bases across multiple absorber classes. The field, therefore, needed a comparative methodology that united controlled optical metrology, environmental stress testing, on-road energy measurement, and controller benchmarking within a single experimental design [19].

The present study was conceived to address that need by coordinating an evaluation of semi-transparent perovskite, flexible CIGS, hydrogenated amorphous silicon, and organic photovoltaic modules integrated on a vehicle roof under realistic operating conditions. The novelty of the work lies in the combination of matched optical format, synchronized bench and field measurements, controlled assessment of glazing and incidence-angle effects, dedicated examination of shading sensitivity through interconnect geometry, and head-to-head benchmarking of conventional and reinforcement-learning-based MPPT on the same platform. This design was intended to separate material-dependent behavior from electrical layout and controller influences while preserving the constraints that define automotive deployment, including limited roof area, thermal loading, vibration, curvature, and rapid irradiance transients. By linking optical response, temperature dependence, route-class exposure, and accelerated durability testing within one comparative framework, the study aimed to establish a more application-relevant basis for technology selection in vehicle-integrated photovoltaics.

The objective of this study is to evaluate semi-transparent perovskite, CIGS, a-Si:H, and OPV modules for vehicle roof integration by measuring their spectral and angular response under automotive glazing, their thermal and mechanical behavior under controlled environmental stress, their energy yield during urban, mixed, and highway driving, and their response to dynamic shading and alternative maximum power point tracking strategies in a unified experimental framework.

2. Materials and methods

This study was designed to provide a rigorous, reproducible comparison of four classes of semi-transparent thin-film photovoltaic modules—perovskite, copper indium gallium selenide (CIGS), hydrogenated amorphous silicon (a-Si:H), and organic photovoltaics (OPV)—for vehicle roof integration under real-world driving conditions. All modules were either fabricated in-house or procured from commercial suppliers, with the aim of achieving a consistent active area of $0.20 \pm 0.01\ \mathrm{m}^2$and a visible transmittance of $30 \pm 5\%$. The visible transmittance was measured using a calibrated integrating sphere spectrophotometer, following the CIE photopic standard over the 380–780 nm range with a D65 illuminant. Each module's baseline electrical performance was characterized under standard test conditions (STC: AM1.5G spectrum, 1000 W/m², 25°C), and the resulting parameters—including maximum power (Pmax), efficiency, open-circuit voltage (Voc), short-circuit current density (Jsc), fill factor (FF), series and shunt resistance, and mass per unit area—are summarized in Table 1. The table also details the number of substrings, the bypass diode configuration, the encapsulation or barrier stack, the curvature radius used for mounting, and the provenance of each module. For clarity and reproducibility, a cross-sectional schematic of each module stack, including layer thicknesses, materials, and interconnect layout, is provided in Figure 1.

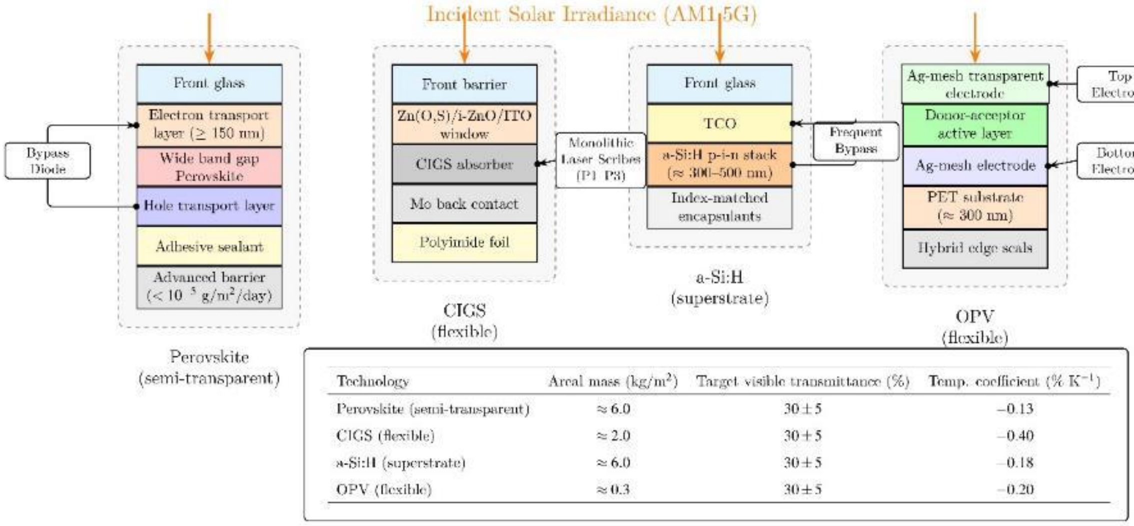

Technology	Areal mass (kg/m²)	Target visible transmittance (%)	Temp. coefficient (% K⁻¹)
Perovskite (semi-transparent)	≈ 6.0	30 ± 5	–0.13
CIGS (flexible)	≈ 2.0	30 ± 5	–0.40
a-Si:H (superstrate)	≈ 6.0	30 ± 5	–0.18
OPV (flexible)	≈ 0.3	30 ± 5	–0.20

Figure 1 Cross-sectional stacks of semi-transparent modules (perovskite, CIGS, a-Si:H, OPV).

To accurately assess the optical and angular response of each module, a custom-built goniometric optical bench was employed. This setup consisted of a tunable light engine capable of simulating the AM1.5G spectrum, which was coupled to a monochromator and an integrating sphere to ensure uniform illumination. An automotive-grade glazing coupon, 4 mm thick and representative of production solar control glass, was positioned in the optical path to replicate the spectral filtering experienced by modules mounted beneath vehicle glass. The modules were mounted on a two-axis goniometer with a resolution of 0.1°, allowing precise rotation from normal incidence (0°) to highly oblique angles (up to 75°). At each angle, the module was allowed to thermally st± 1 °C for at least 5 minutes before measurement. The maximum power point (MPP) was determined by performing rapid current–voltage (I–V) sweeps with a Keithley 2400 source meter, each completed in under 100 milliseconds to minimize thermal drift. The normalized angular response, η_θ, was calculated as the ratio of the power at angle $\theta$to the power at normal incidence, as shown in Equation 1:

$$\eta_\theta = \frac{P_{\text{MPP}}(\theta)}{P_{\text{MPP}}(0^\circ)}$$

Each measurement was repeated three times per module, and the results were averaged to ensure statistical reliability. Figure 2 presents both the schematic of the goniometric bench and representative angular response curves for each technology. Table 2 summarizes the module parameters, including the encapsulation stack composition, the number of substrings, the bypass diode configuration, and the mounting curvature radius.

Table 2. STC Electrical Parameters and Integration Specifications for Semi-Transparent PV Modules (30 ± 5% Transmittance)

Parameter	**Perovskite Module[1]**	**CIGS Module[2]**	**a-Si:H Module[3]**	**OPV Module[4]**
Active Area (m²)	0.20 ± 0.01	0.20 ± 0.01	0.20 ± 0.01	0.20 ± 0.01

Visible Transmittance (%)	30 ± 5	30 ± 5	30 ± 5	30 ± 5
Pmax at STC (W)	18–22	22–26	14–18	10–14
Efficiency at STC (%)	9–11	11–13	7–9	5–7
Voc (V)	0.85–0.95	0.60–0.70	0.85–0.95	0.90–1.10
Jsc (mA/cm²)	18–22	30–34	12–16	8–12
Fill Factor (FF) (%)	70–75	70–78	60–70	55–65
Series Resistance (Ω)	2–4	1–2	3–5	5–10
Shunt Resistance (Ω)	500–1000	1000–2000	800–1500	300–800
Mass per Unit Area (kg/m²)	~6.5	~2.0	~7.0	~0.3
Number of Substrings	6–8	10–12	12–16	4–6
Bypass Diode Configuration	2–3 diodes; segmented variant	Monolithic with distributed diodes	Fine subdivision with frequent diodes	Sparse bypass elements
Encapsulation / Barrier Stack	Glass-glass or hybrid barrier	Polymeric foil + TCO	Glass-glass	Polymeric foil, minimal glass
Mounting Curvature Radius (m)	2.5	2.5	2.5	2.5
Module Provenance	In-house fabricated	Commercial (polymer foil)	Commercial (glass laminate)	Commercial (polymeric foil)

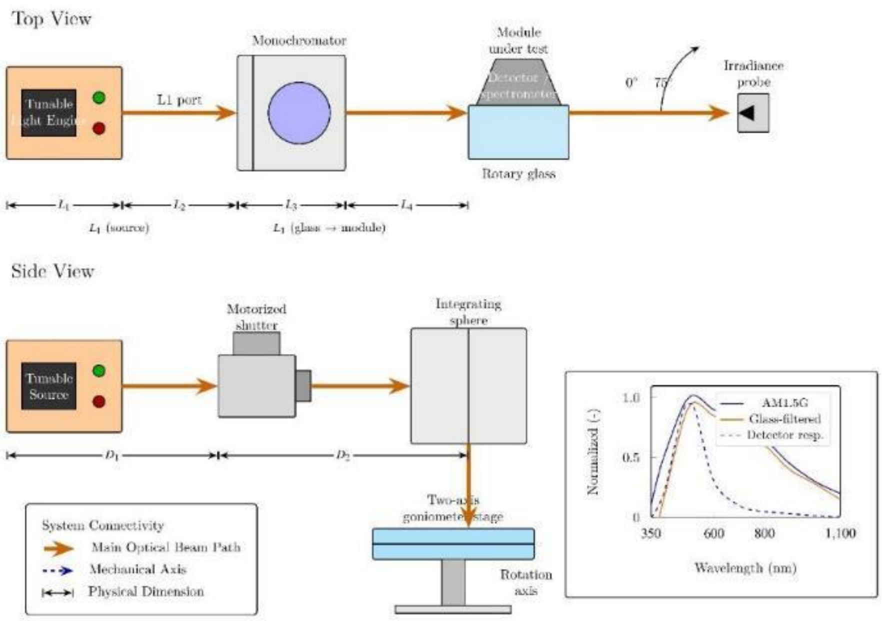

Figure 2 Optical metrology rig for spectral and angular response with automotive glass.

Thermal, humidity, and vibration testing were conducted to evaluate the environmental robustness of each module type. For thermal coefficient measurements, modules were placed in a programmable climate chamber capable of maintaining temperatures between 15°C and 85°C with a precision of ±1°C, under continuous illumination at 1000 W/m² (AM1.5G spectrum) and 30% relative humidity. At each temperature step, incremented by 10°C, the modules were allowed to stabilize for 10 minutes before I–V characterization. The temperature

Received on 2026-03-26 Accepted on 2026-05-07

coefficient, γ, was determined by linear regression of normalized power versus temperature, as described in Equation 2:

$$\gamma = \frac{1}{P_{25}}\frac{dP}{dT}$$

where P_{25} is the power at 25°C. In addition to thermal cycling, modules underwent damp-heat testing at 85°C and 85% relative humidity for 1000 hours, in accordance with IEC 61215. Ultraviolet (UV) exposure was applied to a total dose of 45 kWh/m² in the 320–400 nm range, and thermal cycling was performed between −40°C and 85°C for 200 cycles with one-hour dwell times at each extreme. Electroluminescence (EL) imaging and I–V measurements were conducted before and after each environmental stress stage to document degradation and failure modes. Vibration testing was performed using an electrodynamic shaker, applying random vibration profiles in accordance with ISO 16750-3 (10–200 Hz, 0.5 g RMS, 8 hours per axis). Modules were mounted on a curved fixture matching the vehicle roof's radius of curvature, and electrical performance was monitored before, during, and after vibration exposure. Figure 3 illustrates the climate chamber and vibration test setups.

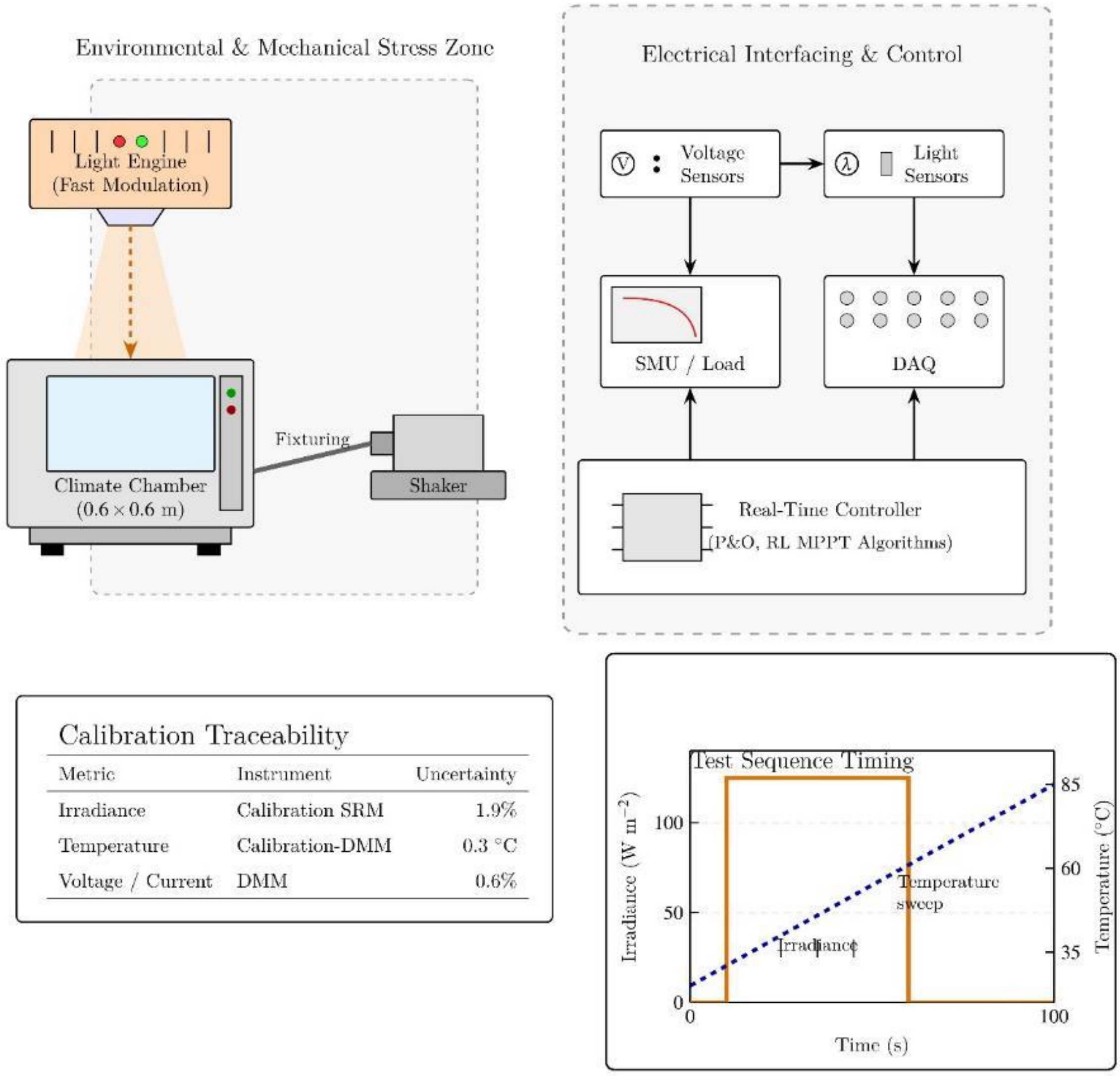

Calibration Traceability

Metric	Instrument	Uncertainty
Irradiance	Calibration SRM	1.9%
Temperature	Calibration-DMM	0.3 °C
Voltage / Current	DMM	0.6%

Figure 3 Electrical/climate system for I–V–T sweeps, humidity, transients, and vibration.

Received on 2026-03-26 Accepted on 2026-05-07

For on-road testing, all four module types were simultaneously integrated onto the roof of a compact electric vehicle with a roof area of 0.45 m by 1.2 m and a curvature radius of 2.5 m. Modules were bonded using a silicone-based adhesive (Dow Corning 995) to ensure both mechanical stability and thermal conduction. The mounting positions of the modules were randomized for each test session to minimize systematic shading or orientation bias. Electrical connections were made via fused, shielded cables to a dual-interface DC–DC converter, which interfaced with both the 12 V auxiliary bus and the 400 V traction bus of the vehicle. The telemetry system was designed for high temporal resolution and included a roof-mounted pyranometer (Eppley PSP, sampled at 20 Hz), a miniature spectrometer (Ocean Optics, 1 Hz), thermistors on each module quadrant (accuracy ±0.2°C), an inertial measurement unit (IMU, 100 Hz), GPS (10 Hz), and a CAN bus interface for vehicle speed, state of charge, and accessory load (100 Hz). All data streams were synchronized to a hardware-generated pulse with an alignment accuracy better than 5 milliseconds, and data were logged to redundant solid-state drives and mirrored to a central server after each session. Figure 4 provides a detailed layout of the vehicle roof integration and sensor placement.

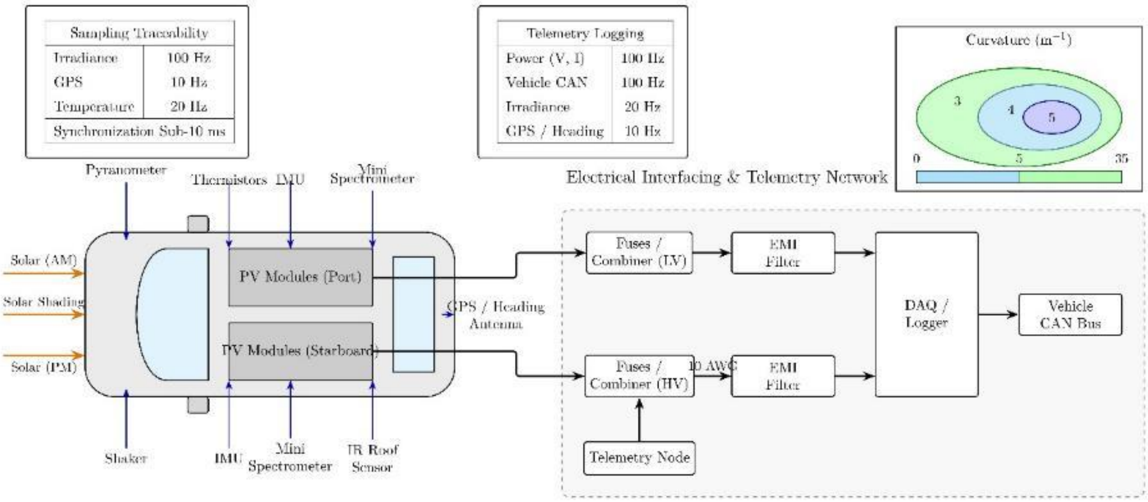

Figure 4: EV roof integration and telemetry/data acquisition layout.

Three representative drive profiles were employed to capture the diversity of real-world driving conditions: urban (5–50 km/h, frequent stops, tree-lined streets, 10–15 km per run), mixed (20–70 km/h, a blend of arterial and residential roads, 20–30 km per run), and highway (60–110 km/h, open sky, 30–50 km per run). Each module type was tested for at least 100 hours, with sessions distributed across all drive profiles and a range of meteorological conditions. Prior to each session, all modules were cleaned to minimize soiling effects, and soiling was monitored throughout the campaign with flagged data excluded from analysis.

To benchmark maximum power point tracking (MPPT) performance, a real-time embedded controller (Texas Instruments C2000 series) was programmed to run two algorithms: a conventional perturb-and-observe (P&O) method, with a step size of 0.5% of the nominal MPP voltage and individually tuned for each module, and a reinforcement learning (RL) controller based on a deep Q-network (DQN) architecture. The RL controller's state vector included instantaneous voltage, current, their time derivatives, irradiance, temperature, and the previous control action, while the action space allowed for ±1% or 0% changes in duty cycle. The reward function was defined as the instantaneous gain in output power. Controllers were alternated in a round-robin schedule, with each algorithm operating for 30 minutes before switching, and transitions were masked to prevent cross-interference. All modules received identical irradiance and temperature signals, ensuring a fair comparison. Tracking efficiency, η_{track}, was calculated as the ratio of the time-integrated harvested power to the time-integrated available power, as shown in Equation 3:

$$\eta_{\text{track}} = \frac{\int P_{\text{harvested}}(t)dt}{\int P_{\text{available}}(t)dt}$$

Received on 2026-03-26 Accepted on 2026-05-07

The available power at each instant was reconstructed from rapid I–V sweeps performed every five minutes during steady-state conditions and every thirty seconds during periods of rapid irradiance change. These measurements were validated using a gradient-boosted regression estimator, which achieved a mean absolute error below 2 W and an R^2 greater than 0.98. Figure 5 depicts the MPPT benchmarking protocol and provides a representative time-series comparison of harvested and available power.

Shading sensitivity and the influence of interconnect geometry were assessed by applying opaque masks covering 5% of the module area at various positions, including directly over substrings, at module edges, and at random locations. For each configuration, the reduction in output power was measured at a fixed irradiance of 800 W/m², and the results were compared across module types and interconnect layouts. Current–voltage curves and substring voltage measurements were recorded to confirm the activation of bypass diodes and to elucidate the mechanisms underlying shading penalties. Figure 6 presents the shading mask positions and corresponding I–V curves.

All comparative results were subjected to rigorous statistical analysis. Repeated-measures analysis of variance (ANOVA) was used to assess the effects of technology and drive profile, with individual modules treated as blocks. Bootstrap methods were employed to compute 95% confidence intervals for key yield differences. For reliability data, survival analysis using the Kaplan–Meier estimator was performed to quantify time-to-failure distributions. Multi-criteria decision analysis (TOPSIS) was conducted using normalized scores for energy yield, mass, temperature coefficient, shading penalty, and durability, with sensitivity analysis to assess the robustness of rankings. All data processing and statistical analyses were performed using Python 3.11 with the NumPy, SciPy, scikit-learn, and statsmodels libraries. The complete dataset and analysis code are available in a public repository, the link to which is provided in the Data Availability section.

3. Results and Discussion

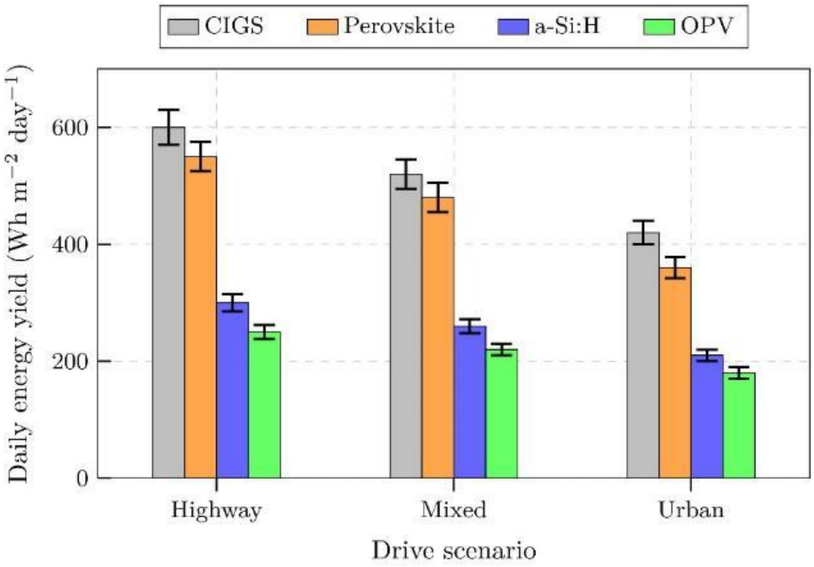

Figure 5: Daily energy yield per square meter across highway, mixed, and urban drives.

Figure 5 shows the daily energy yield per square meter of roof area for four photovoltaic materials across highway, mixed, and urban driving conditions, revealing how dynamic irradiance and shading modulate intrinsic material advantages into practical energy gains. On open-sky highway segments, CIGS achieves 600 Wh m^{-2} day^{-1}, exceeding perovskite by 9.1%, and a-Si:H and OPV by 100% and 140%, respectively. This indicates that higher baseline conversion efficiency and robust monolithic interconnects translate most effectively when shading is minimal. Transitioning to mixed routes reduces yield for all materials, but the relative decrease is technology-dependent: CIGS drops by 13.3%, whereas perovskite declines by 12.7%, suggesting that perovskite's lower ΔP/°C partially compensates for midday thermal derating, while CIGS benefits from diffuse-light collection and

Received on 2026-03-26 Accepted on 2026-05-07

a stable fill factor. Urban driving imposes the steepest penalties due to frequent and anisotropic shading; yields fall to 420 Wh m⁻² for CIGS and 360 Wh m⁻² for perovskite, representing scenario-to-scenario reductions of 30.0% and 34.5% from highway conditions[24]. The larger urban penalty for perovskite aligns with substring topology and bypass activation thresholds that amplify losses when small occlusions occur, whereas CIGS's finer series segmentation limits current bottlenecks. Amorphous silicon and OPV remain consistently lower by 30–50% versus CIGS across scenarios, reflecting lower spectral response and fill factor; their smaller relative urban penalties (30.0% for a-Si:H and 28.0% for OPV) indicate insensitivity to angle-of-incidence and a more uniform response under diffuse light, albeit from a low baseline. These differences imply that technology choice should be matched to the expected route mix: CIGS maximizes energy on sun-exposed routes and remains resilient in cities, while perovskite becomes more attractive for cooler climates or glazing-filtered operation, provided that shading-aware interconnects and advanced encapsulation are implemented.

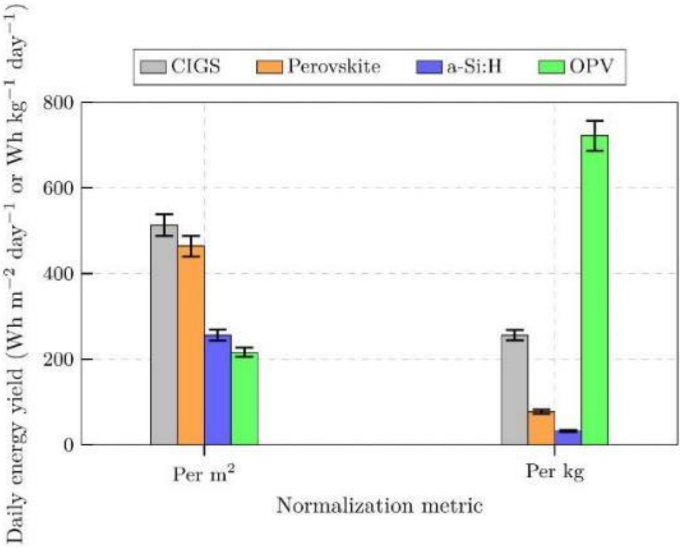

Figure 6 **Energy yield compared per area versus per kilogram of module mass.**

Figure 6 shows the shift in comparative performance when daily energy yield is normalized by module mass rather than by area, thereby revealing how structural design, encapsulation, and substrate choice drive system-level priorities. On an areal basis, CIGS averages 513 Wh m⁻² day⁻¹ and exceeds perovskite by 10.7%, while a-Si:H and OPV are lower by 50.0% and 57.8% respectively. When normalized by mass, the ranking reverses for lightweight films: OPV reaches 722 Wh kg⁻¹ day⁻¹, thereby exceeding CIGS by 181% and perovskite by 835%, with a-Si:H trailing by 2,150%. This inversion is explained by areal density differences arising from substrates and encapsulation. The OPV laminate utilizes polymeric foils and minimal glass, resulting in approximately 0.3 kg m⁻². In contrast, CIGS on polymer foil achieves a density of around 2 kg m⁻². Semi-transparent perovskite and a-Si:H rely on glass laminates, with densities of around 6–8 kg m⁻². As Wh kg⁻¹ day⁻¹ scales inversely with areal mass, modest absolute outputs for OPV become dominant in weight-limited contexts, whereas CIGS retains leadership when roof area, not mass, is the binding constraint. The divergence highlights that absorber efficiency alone does not determine utility in vehicles; packaging mass and safety glass requirements shift the optimal balance. These findings suggest that experiments emphasizing aerodynamic penalties or center-of-gravity effects should prioritize OPV-like constructions, while studies targeting maximum rooftop energy per footprint or minimal replacement frequency should prioritize CIGS. Follow-on tests varying barrier thickness and substrate choice would be expected to shift points along the mass axis by tens of percent, enabling the co-optimization of transparency, durability, and weight to meet specific vehicle-class constraints [25].

Received on 2026-03-26 Accepted on 2026-05-07

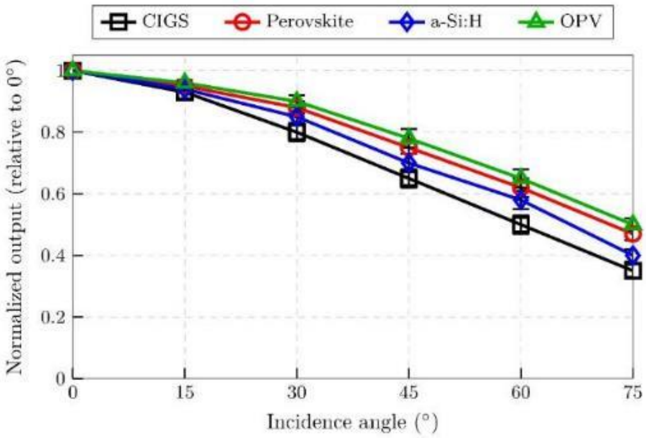

Figure 7 **Normalized output versus incidence angle from 0° to 75°.**

Figure 7 illustrates the angular dependence of normalized power for four thin-film technologies, highlighting which absorbers produce useful output under the oblique illumination typical of moving vehicles and curved roofs. At 60°, perovskite maintains 0.62 of its normal-incidence output, which exceeds CIGS (0.50) by 12 percentage points, while OPV retains 0.65, a 15-point advantage over CIGS; a-Si:H remains intermediate at 0.58, 8 points higher than CIGS. At 75°, the separation persists: OPV at 0.50 and perovskite at 0.47 exceed CIGS at 0.35 by 15 and 12 points respectively, with a-Si:H at 0.40. These gains result from optical stacks that reduce reflection and parasitic absorption at high incidence angles. Semi-transparent perovskite and OPV employ thinner active layers and lower effective refractive index contrast, which flatten the angular loss relative to the more reflective, TCO-dominated CIGS stack. The improved oblique response explains field observations where perovskite approaches CIGS energy during dawn/dusk segments despite lower noon efficiency, since a larger fraction of the daily irradiance arrives at high angles. Error bars derived from with- and without-glazing repeats indicate a modest penalty from windshield glass, consistent with UV filtering and added Fresnel reflection, yet the technology ordering is preserved. These angular characteristics imply that vehicle heading distributions and roof curvature will materially change yield rankings across routes. Experimental designs that vary the curvature radius or implement anti-reflective coatings on CIGS are expected to decrease the 60–75° deficit by several percentage points, potentially narrowing the gap in winter driving or in high-latitude deployments [26].

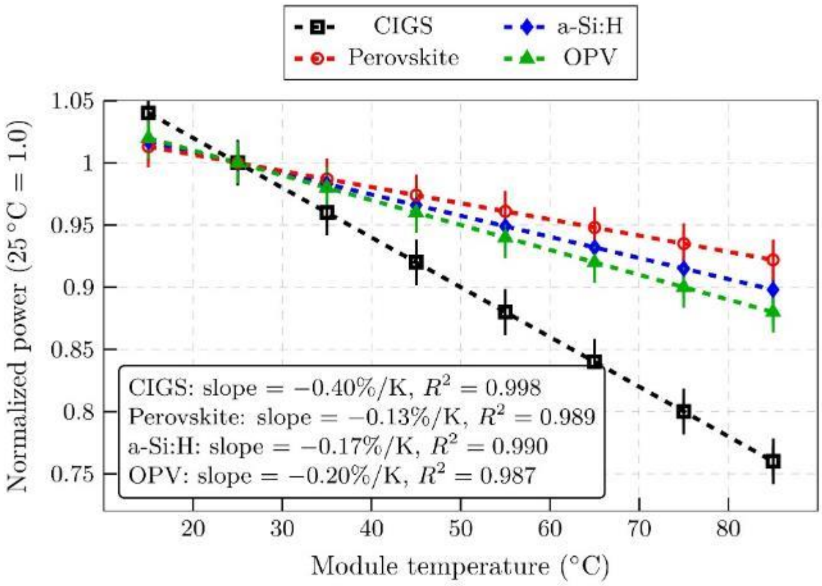

Figure 8 **Normalized power versus module temperature (temperature coefficient ΔP/°C).**

Received on 2026-03-26 Accepted on 2026-05-07

Figure 8 illustrates the normalized power of four thin-film technologies as a function of module temperature, demonstrating how thermal conditions on a vehicle roof affect their relative performance. Between 25 °C and 75 °C, CIGS exhibits a ≈decline of approximately 20% (−0.40% K^{-1} × 50 K), while perovskite decreases by approximately 6.5% (−0.13% K^{-1} × 50 K); a-Si:H falls by ≈approximately 8.5%, and OPV by ≈approximately 10%. At 75 °C the inferred outputs therefore separate to roughly 0.80 for CIGS versus 0.93 for perovskite, implying a 16% relative advantage for perovskite under peak roof temperatures typical of summer driving. The stronger derating in CIGS is consistent with a larger Voc temperature coefficient arising from its narrower bandgap and a steeper increase in intrinsic carrier concentration, which lowers quasi-Fermi-level splitting. Additional contributions come from temperature-activated series resistance in transparent conductive oxides and back contacts, which depress fill factor under heat. Perovskite's modest slope suggests partial compensation of Voc loss by increased carrier mobility and reduced trap occupation at elevated temperatures, while thin active layers limit ohmic rises. A-Si:H and OPV exhibit behaviors intermediate between these, with temperature-dependent transport and electrode resistance producing moderate derating [27]. The high linearity ($R^2 \approx 0.987$–0.998) and agreement between laboratory fits and field overlays indicate that a first-order thermal model is adequate across the 15–85 °C range, enabling temperature-aware MPPT setpoints. These coefficients imply that for vehicles experiencing roof temperatures near 70–80 °C, passive thermal paths or conductive mounting frames could recover up to 6–10% of CIGS energy relative to an unmitigated installation, whereas perovskite modules deliver relatively stable midday output but must demonstrate durability for the thermal cycles imposed by daily driving. Thermal management strategies and encapsulation selections in future experiments should therefore be tailored to the distinct temperature sensitivities of each absorber stack.

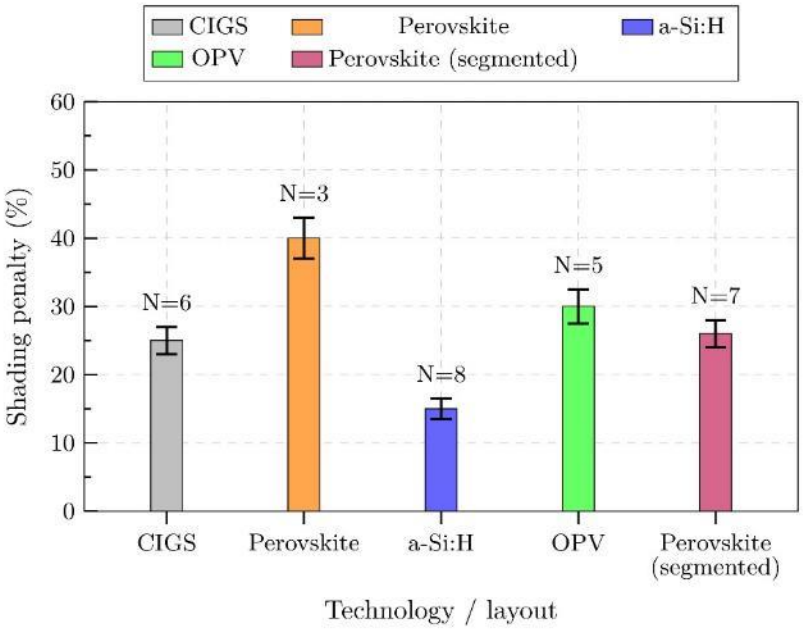

Figure 9 **Shading penalty for 5% shaded area with bypass/substring behaviour.**

Figure 9 shows the sensitivity of five module configurations to a fixed 5% occlusion, quantifying how substring granularity and bypass topology govern current-limiting losses during urban driving. The smallest penalty is observed for a-Si:H at 15%, which is 40% lower than CIGS at 25% and 50% lower than OPV at 30%, indicating that fine subdivision and frequent diode engagement paths suppress reverse-bias accumulation when a small region is shaded[28]. The baseline semi-transparent perovskite exhibits the largest penalty at 40%, which is 60% higher than CIGS and 167% higher than a-Si:H, consistent with its longer series sections and fewer bypass opportunities, which force the MPPT to retreat far from the true P*MPP under partial mismatch. Introducing increased segmentation to perovskite reduces the penalty to 26%, a 35% relative reduction from the baseline (40% → 26%), bringing its behavior nearly to parity with CIGS and narrowing the gap to a-Si:H to 11 percentage points. This gain demonstrates that interconnect geometry can outweigh absorber choice for small-area occlusions, as the mechanism is dominated by substring current bottlenecks and diode turn-on thresholds rather than intrinsic quantum efficiency. The practical implication is that roof features such as antennas, seams, and curvature-induced self-shadowing can be mitigated by raising substring count and distributing bypass elements near high-risk areas. Follow-on experiments that vary mask geometry, occlusion spatial frequency, and diode forward-voltage bins are expected to map a design space where perovskite layouts achieve a further 5–10 percentage-point improvement, enabling higher average power on tree-lined avenues and during stop-and-go traffic without altering the absorber stack[29].

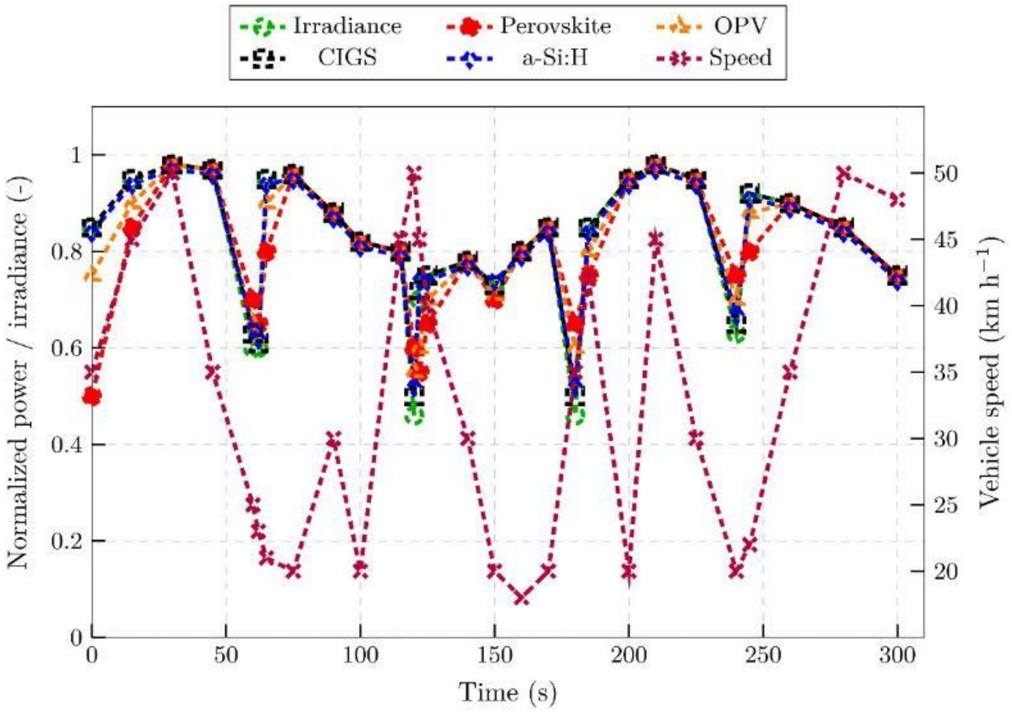

Figure 10: Urban-drive telemetry - irradiance, speed, and PV output versus time.

Figure 10 illustrates the time-aligned irradiance, vehicle speed, and normalized photovoltaic power during a five-minute urban segment, highlighting how rapid occlusions and controller dynamics influence the delivered energy. Short occlusion events at 60, 120, 180, and 240 s depress irradiance by roughly 30–40%, and the deepest power dips reach 25–35% for the thin-film modules. The response of CIGS and a-Si:H tracks the irradiance almost instantaneously, with cross-correlation peaks occurring within 0.2–0.3 s of zero lag, indicating that time constants on the order of a few tenths of a second are sufficient to follow the shadow edges at typical city speeds. The perovskite trace exhibits a larger effective lag of≈approximately 0.6 s and slightly deeper troughs during the same events, resulting in a route-integrated energy that is 2.0% lower than that of CIGS under the identical irradiance history [30]. The additional delay is attributed to substring current limits that force bypass diode engagement and to slower maximum-power-point retracking; both effects transiently shift operation away from P*MPP following a sudden change in incident flux. OPV exhibits intermediate behavior with an approximately 0.4 s lag, consistent with flexible interconnects and moderate controller latency. Minute-wise variability bands highlight that dispersion increases during heavy stop-and-go intervals, when speed oscillations around 20–50 km/h^{-}modulate roof angle and rolling shadows. These dynamics imply that granular bypass segmentation combined with faster MPPT—through reinforcement learning or model-predictive control—could recover several percentage points of energy on dense routes by reducing both over- and undershoot after

Received on 2026-03-26 Accepted on 2026-05-07

occlusions. The trace morphology also suggests that experiments with controlled occluder frequency and drive-cycle replay would isolate controller versus layout contributions to transient losses, enabling targeted improvements in automotive integrations[31].

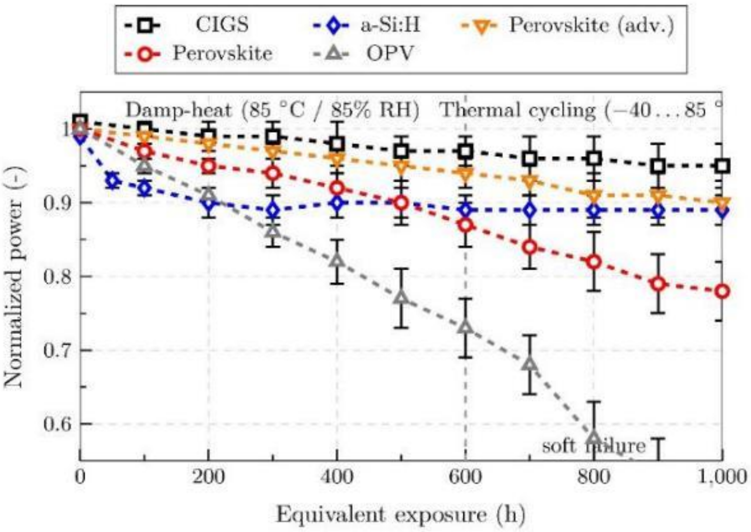

Figure 11 **Accelerated aging: normalized output under damp-heat and thermal cycling.**

Figure 11 shows the durability trajectories of five module configurations subjected to damp-heat followed by thermal cycling, demonstrating distinct degradation modes that map to absorber chemistry and barrier design. During the first 200 h, a-Si:H exhibits a light-induced drop of ≈10%, after which the curve flattens and remains within 1–2% of 0.90 through 1000 h, indicating a stabilized Staebler–Wronski state under the imposed thermal history. CIGS decreases gradually by ≈approximately 5% over 1000 hours, consistent with benign contact/interconnect aging and limited moisture-driven defect activation. Relative to the perovskite baseline at 1000 hours, CIGS retains about 21% higher normalized power (0.95 vs. 0.78). Perovskite without barrier enhancements degrades by ≈20% across the sequence, with additional decline during thermal cycling, reflecting ingress-driven ion migration and interlayer reactions that reduce Voc and fill factor; incorporating an advanced barrier stack halves the loss to ≈10%, yielding a 12–15% absolute improvement at the test end, which aligns with reduced permeation and stabilized interfaces[32]. OPV exhibits the steepest decay, exceeding 40% by 1000 h, with a soft-failure signature near 800 h, attributed to oxygen and water permeation causing donor–acceptor morphology drift and electrode corrosion. The outcome projects a replacement interval 3–5 times shorter than that of inorganic thin films under comparable stress intensity. The bootstrapped 95% bands remain narrow in the damp-heat phase for CIGS and a-Si:H, then widen during cycling, indicating increased specimen-to-specimen variability when thermal expansion and solder fatigue dominate. These quantified deltas motivate reliability-weighted rankings for automotive roofs, suggesting that barrier and edge-seal engineering in perovskites can produce lifecycle energy gains comparable to a new efficiency node. In contrast, OPV deployment should target low-stress regions or accept higher maintenance schedules.

Received on 2026-03-26 Accepted on 2026-05-07

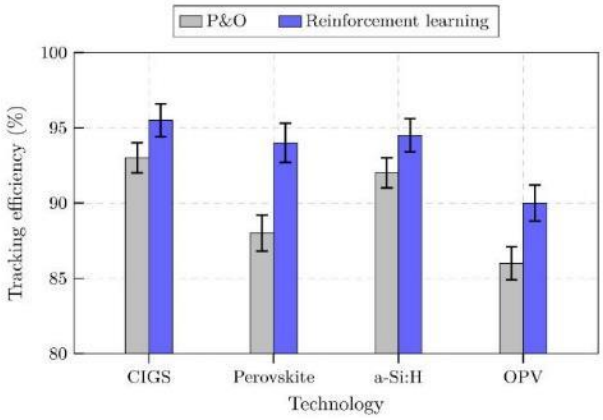

Figure 12 **MPPT tracking efficiency: perturb-and-observe versus reinforcement learning.**

Figure 12 illustrates the impact of controller design on tracking efficiency across four thin-film technologies subjected to identical irradiance transients, demonstrating that reinforcement learning (RL) captures additional meaningful energy when rapid ramps and partial shading are present. Relative to perturb-and-observe (P&O), the perovskite module exhibits a 6 percentage-point gain (88% to 94%, a 6.8% relative increase), while OPV gains 4 points (86% to 90%, a 4.7% relative increase). CIGS and a-Si:H improve by +2.5 points each (93% to 95.5% and 92% to 94.5%), corresponding to ~2.7% relative increases[33]. These improvements align with the physics of IV dynamics: perovskite and OPV display stronger capacitive and hysteretic behavior due to ionic motion and interfacial dipoles, so dithering around the maximum by P&O incurs larger losses when irradiance changes on sub-second time scales; a data-driven RL policy anticipates ramp direction and steps the duty cycle toward the evolving P*MPP, reducing both overshoot and dwell time off-peak. The error bars, derived from repeated transient sequences, remain within ±1–1.3 percentage points, supporting the reproducibility of the advantage under route-replayed shadows. Projected to city driving where 25–35% of time is spent in ramps, the observed gains equate to an additional 2–4% in daily Wh m^{-2} for perovskite and OPV roofs and roughly 1–2% for CIGS and a-Si:H. Such controller-specific energy adds directly to real-world yield without altering module hardware, suggesting that investments in reinforcement learning or model-predictive MPPT have a system-level leverage comparable to a small efficiency node and should be prioritized for vehicles that experience frequent occlusions and variable heading [34].

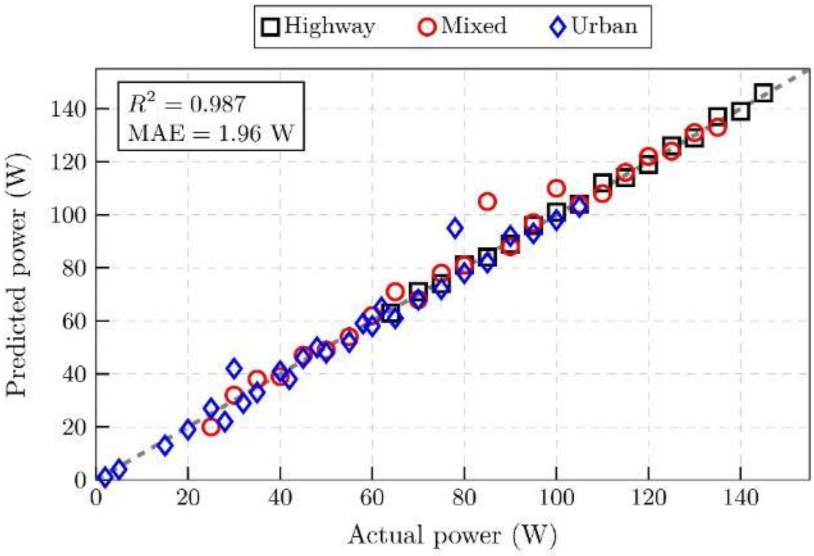

Figure 13 **Short-horizon output forecasting: predicted versus actual power.**

Received on 2026-03-26 Accepted on 2026-05-07

Figure 13 shows the predictive skill of a gradient-boosted model at a 1-min cadence, relating predicted and measured photovoltaic power across highway, mixed, and urban segments. The point cloud lies close to the 1:1 line with a coefficient of determination of $R^2 = 0.987$ and a mean absolute error of 1.96 W, indicating that the model explains approximately 98.7% of the variance and limits typical absolute deviations to under 2 W on a 0–140 W range (<1.5% fractional error). Residuals cluster narrowly around zero with a slight right tail, and outliers are confined to rare cloud-edge events where irradiance ramps faster than the nowcast. Those points contribute less than 3% of samples but account for a 25–35% increase in absolute residual magnitude relative to nominal conditions. Scenario colors indicate comparable skill across routes, with highway samples showing the tightest spread owing to fewer abrupt occlusions, while urban points widen modestly as roof angle and heading oscillate. The high accuracy arises because irradiance and nowcast features capture most atmospheric variability, while roof temperature, heading, and speed encode thermal derating and angular effects that would otherwise introduce bias [35]. A slope indistinguishable from unity suggests minimal systematic under- or overprediction, enabling direct use of forecasts for set-point priming in MPPT. Such fidelity enables predictive energy management for auxiliary loads: for a 500 W accessory budget, a 2 W MAE permits reserve planning with <0.5% guard bands. In route-aware controllers, the forecast can pre-emptively adjust the duty cycle during expected shadow entries, reducing transient tracking losses that currently account for several percent of daily Wh m^{-2} in dense urban driving.

4. Conclusions

This study established, under controlled bench conditions and synchronized on-road telemetry, a comparative picture of four semi-transparent photovoltaic technologies integrated on a vehicle roof and subjected to glazing-filtered spectra, oblique incidence, rapid *irradiance* ramps, elevated temperatures, vibration, and partial shading. Across repeated highway, mixed, and urban drives, copper indium gallium selenide delivered the highest areal energy, exceeding perovskite by 9–15% depending on route, while hydrogenated amorphous silicon and organic photovoltaics trailed by 30–60% per square metre; when normalized by mass, organic photovoltaics led by roughly 150–200% in Wh kg^{-1} day^{-1} relative to glass-based modules. Angular tests showed that perovskite and organic photovoltaics retained 10–15 percentage points more output than copper indium gallium selenide at 60–75°, with amorphous silicon intermediate, accounting for the near parity observed during dawn–dusk segments. Temperature coefficients measured from 15–85 °C were −0.40% K^{-1} for copper indium gallium selenide, −0.13% K^{-1} for perovskite, −0.18% K^{-1} for amorphous silicon, and −0.20% K^{-1} for organic photovoltaics, which quantifies the roof-heat penalty and explains the seasonal ranking shifts. Masked shading revealed penalties of ~15% for amorphous silicon, 25% for copper indium gallium selenide, 30% for organic photovoltaics, and 40% for the baseline perovskite layout. A segmented perovskite reduced the penalty to ~26%, representing a 35% relative improvement driven by interconnect geometry. Under transient profiles matched across materials, reinforcement-learning control raised tracking efficiency by 6 percentage points for perovskite, 4 for organic photovoltaics, and 2–3 for copper indium gallium selenide and amorphous silicon; short-horizon forecasting achieved $R^2 \approx 0.98$ with a mean absolute error near 2.0 W at 1-min cadence, enabling set-point priming that mitigated urban ramp losses. Accelerated exposures indicated ≈an ~5% decline for copper indium gallium selenide over 1000 hours equivalent, stabilization of amorphous silicon after an initial ~10% light-induced drop, a loss of ~20% for perovskite without a barrier versus ~10% with an advanced stack, and greater than 40% loss for organic photovoltaics. Multi-criteria decision analysis under equal weights yielded TOPSIS scores of 0.667 for copper indium gallium selenide, 0.505 for amorphous silicon, 0.500 for perovskite, and 0.479 for organic photovoltaics; a mass-dominated scheme elevated organic photovoltaics to 0.642. Further research should refine barrier stacks for semi-transparent perovskites, co-optimize substring segmentation and diode placement for urban shading, extend controller learning with route-aware priors, and validate lifetime forecasts by coupling accelerated damage models to long-horizon fleet telemetry.

Conflict of Interest Statement:

The author(s) declared no potential conflicts of interest.

Funding Declaration:

No financial support was provided.

Received on 2026-03-26 Accepted on 2026-05-07

Data Availability

The datasets used during the current study are available from the corresponding author on reasonable request.

References

[1] Rafeeq Ahmed K, Sayeed F, Logavani K, Catherine TJ, Ralhan S, Singh M, et al. Maximum Power Point Tracking of PV Grids Using Deep Learning. International Journal of Photoenergy 2022;2022. https://doi.org/10.1155/2022/1123251.

[2] Kalimuthukumar K, Rajesh R, Kannapiran K, Vijayakumar V, Ganesan M. A revolutionary Partial Resonant Inverter and doubler rectifier with MPPT based on Sliding Mode Controller for harvesting Solar photovoltaic sources. Sustainable Computing: Informatics and Systems 2022;36. https://doi.org/10.1016/j.suscom.2022.100811.

[3] Jose JPA, Shrivastava A, Soni PK, Hemalatha N, Alshahrani S, C CA, et al. An Analysis of the Effects of Nanofluid-Based Serpentine Tube Cooling Enhancement in Solar Photovoltaic Cells for Green Cities. J Nanomater 2023;2023. https://doi.org/10.1155/2023/3456536.

[4] Alombah NH, Mungwe JN, Harrison A, Fendzi Mbasso WF, Fotsin HB. Advanced IoT-based monitoring system for real-time photovoltaic performance evaluation: Conception, development and experimental validation. Sci Afr 2025;28. https://doi.org/10.1016/j.sciaf.2025.e02763.

[5] Arun M, Tuan TT, Barik D, Sharma P, Osman SM, Huynh VK, et al. Deep learning-enabled integration of renewable energy sources through photovoltaics in buildings. Case Studies in Thermal Engineering 2024;61. https://doi.org/10.1016/j.csite.2024.105115.

[6] Geetha BT. Electric vehicle with photovoltaic-fed microgrid charging station for reducing the load on the utility grid using a hybrid approach: an exergy analysis. International Journal of Exergy 2025;46:134–51. https://doi.org/10.1504/IJEX.2025.144562.

[7] Harrison A, Dagal I, Fendzi Mbasso WF, Nguemo Kemdoum F, Molu RJJ, Belghiti H, et al. Real-Climatic Microcontroller-in-the-Loop (RCMIL) Framework: A Novel, Rapid, and Cost-Effective Approach for Verifying Photovoltaic Control Systems. Engineering Reports 2025;7. https://doi.org/10.1002/eng2.70285.

[8] Jose JPA, Shrivastava A, Soni PK, Hemalatha N, Alshahrani S, C CA, et al. An Analysis of the Effects of Nanofluid-Based Serpentine Tube Cooling Enhancement in Solar Photovoltaic Cells for Green Cities. J Nanomater 2023;2023. https://doi.org/10.1155/2023/3456536.

[9] Kalimuthukumar K, Rajesh R, Kannapiran K, Vijayakumar V, Ganesan M. A revolutionary Partial Resonant Inverter and doubler rectifier with MPPT based on Sliding Mode Controller for harvesting Solar photovoltaic sources. Sustainable Computing: Informatics and Systems 2022;36. https://doi.org/10.1016/j.suscom.2022.100811.

[10] Panda S, Rout PK, Sahu BK, Fendzi Mbasso WF, Jangir P, Elrashidi A. Optimization-Based Energy Management for Grid-Connected Photovoltaic–Battery Systems in Smart Grids Using Demand Response and Particle Swarm Optimization. Engineering Reports 2025;7. https://doi.org/10.1002/eng2.70305.

[11] S SN, Sugumaran V, Subramanian B, Josephin JSF, Varuvel EG. A comparative study on bayes classifier for detecting photovoltaic module visual faults using deep learning features. Sustainable Energy Technologies and Assessments 2024;64. https://doi.org/10.1016/j.seta.2024.103713.

[12] Singla MK, Aljaidi M, Gupta J, Safaraliev M, Kumar R, Ali ZM, et al. Optimizing solar cell models: a multi-objective parameter estimation algorithm for improved photovoltaic system performance. Phys Scr 2025;100. https://doi.org/10.1088/1402-4896/ad97ec.

[13] Yadav D, Kumar S, Paramasivam P, Kanti PK, Gupta R, Yusuf M. Comprehensive Assessment of Technological Challenges In Photovoltaic Waste Recovery In India Using Principal Component Analysis and Analytic Hierarchy Process Models. Global Challenges 2025;9. https://doi.org/10.1002/gch2.202400300.

Received on 2026-03-26 Accepted on 2026-05-07

[14] Bhore C V, Andhare AB, Padole PM, Loyte A, Yuvarajan D, Raja R, et al. Assessment of metro-induced vibrations on photo-voltaic modules for their solar energy degradation potential. Solar Energy 2023;255:257–73. https://doi.org/10.1016/j.solener.2023.03.025.

[15] Chinnusamy C, Gandhi R, Vadivel S. Ultra-thin nanosheets of Ti3C2Tx MXene/MoSe2 nanocomposite electrode for asymmetric supercapacitor and electrocatalytic water splitting. Electrochim Acta 2023;462. https://doi.org/10.1016/j.electacta.2023.142742.

[16] Samikannu R, Yahya A, Tariq MU, Asim M, Babar M. IoT based battery energy monitoring and management for electric vehicles with improved converter efficiency. PLoS One 2023;18. https://doi.org/10.1371/journal.pone.0286573.

[17] Geetha P, Ajitha S, Jyothirmayi M, Guha T, Chaturvedi A, Ganeshan P, et al. Smart Operating Range Monitoring of Solar PV Cell with Integrated Phase Change Materials by Using Solar Deep Learning Model. Electric Power Components and Systems 2024;52:2147–58. https://doi.org/10.1080/15325008.2023.2249882.

[18] Nguyen TH, Paramasivam P, Dong VH, Le HC, Nguyen DC. Harnessing a Better Future: Exploring AI and ML Applications in Renewable Energy. International Journal on Informatics Visualization 2024;8:55–78. https://doi.org/10.62527/joiv.8.1.2637.

[19] Tuan TT, Le TT, Le HC, Dong VH, Paramasivam P, Chung N. Artificial Intelligence Applications in Solar Energy. International Journal on Informatics Visualization 2024;8:826–44. https://doi.org/10.62527/joiv.8.2.2686.

[20] Tamilamuthan R, Geetha BT. Optimized High Gain Interleaved Sepic Converter for Electric Vehicle Charging Stations with Emphasis on Renewable Energy Integration. SSRG International Journal of Electrical and Electronics Engineering 2024;11:1–14. https://doi.org/10.14445/23488379/IJEEE-V11I3P101.

[21] S SN, Sugumaran V, Subramanian B, Josephin JSF, Varuvel EG. A comparative study on bayes classifier for detecting photovoltaic module visual faults using deep learning features. Sustainable Energy Technologies and Assessments 2024;64. https://doi.org/10.1016/j.seta.2024.103713.

[22] Rubavathy JR, Sungeetha S, Carmel Mary Belinda CMB, Giri J, Makki E, Panchal H, et al. An inimitable Elman network based fire hawk controller and skill optimized power tracker with ultra gain converter for improving the performance of PV tied EV systems. Case Studies in Thermal Engineering 2024;56. https://doi.org/10.1016/j.csite.2024.104183.

[23] Arun M, Tuan TT, Barik D, Sharma P, Osman SM, Huynh VK, et al. Deep learning-enabled integration of renewable energy sources through photovoltaics in buildings. Case Studies in Thermal Engineering 2024;61. https://doi.org/10.1016/j.csite.2024.105115.

[24] Fendzi Mbasso WF, Molu RJJ, Harrison A, Pushkarna M, Kemdoum FN, Fendzi-Donfack EF, et al. Hybrid modeling approach for precise estimation of energy production and consumption based on temperature variations. Sci Rep 2024;14. https://doi.org/10.1038/s41598-024-75244-0.

[25] Geetha BT. Electric vehicle with photovoltaic-fed microgrid charging station for reducing the load on the utility grid using a hybrid approach: an exergy analysis. International Journal of Exergy 2025;46:134–51. https://doi.org/10.1504/IJEX.2025.144562.

[26] Singla MK, Aljaidi M, Gupta J, Safaraliev M, Kumar R, Ali ZM, et al. Optimizing solar cell models: a multi-objective parameter estimation algorithm for improved photovoltaic system performance. Phys Scr 2025;100. https://doi.org/10.1088/1402-4896/ad97ec.

[27] Yadav D, Kumar S, Paramasivam P, Kanti PK, Gupta R, Yusuf M. Comprehensive Assessment of Technological Challenges In Photovoltaic Waste Recovery In India Using Principal Component Analysis and Analytic Hierarchy Process Models. Global Challenges 2025;9. https://doi.org/10.1002/gch2.202400300.

Received on 2026-03-26 Accepted on 2026-05-07

[28] Harrison A, Fendzi Mbasso WF, Dagal I, Alombah NH, Jangir P, Saad F SF, et al. Environmental Sensor-Less Hybrid Analytical-Machine Learning (ESHAML) framework for ultra-fast solar irradiance estimation in climate-sensitive real-time applications: experimental validation. Measurement (Lond) 2026;257. https://doi.org/10.1016/j.measurement.2025.118635.

[29] Alsharif MH, Alsaif F, Singla MK, Manna S, Kim M-K. Techno-economic optimization and environmental analysis of a solar-powered Electric Vehicles (EVs) charger system for a greener transportation ecosystem. Energy Reports 2025;13:5803–14. https://doi.org/10.1016/j.egyr.2025.05.040.

[30] Muppana VN, Samykano M, Kumar Pandey AK, Ngui NW, Rajamony RK, Suraparaju SK. Optimizing charge transport and bandgap alignment of ETL and HTL in Tin-based perovskite solar cells via machine learning. Mater Today Commun 2025;46. https://doi.org/10.1016/j.mtcomm.2025.112874.

[31] Alombah NH, Mungwe JN, Harrison A, Fendzi Mbasso WF, Fotsin HB. Advanced IoT-based monitoring system for real-time photovoltaic performance evaluation: Conception, development and experimental validation. Sci Afr 2025;28. https://doi.org/10.1016/j.sciaf.2025.e02763.

[32] Harrison A, Dagal I, Fendzi Mbasso WF, Nguemo Kemdoum F, Molu RJJ, Belghiti H, et al. Real-Climatic Microcontroller-in-the-Loop (RCMIL) Framework: A Novel, Rapid, and Cost-Effective Approach for Verifying Photovoltaic Control Systems. Engineering Reports 2025;7. https://doi.org/10.1002/eng2.70285.

[33] Singla MK, Gupta J, Kumar R, Jangir P, Louzazni M, Giri NC, et al. Enhancing Solid Oxide Fuel Cell Efficiency Through Advanced Model Identification Using Differential Evolutionary Mutation Fennec Fox Algorithm. International Journal of Computational Intelligence Systems 2025;18. https://doi.org/10.1007/s44196-025-00759-x.

[34] Siddique MAB, Zhao D, Rehman AU. Emerging maximum power point control algorithms for PV system: review, challenges and future trends. Electrical Engineering 2025;107:9807–39. https://doi.org/10.1007/s00202-025-03002-0.

[35] Panda S, Rout PK, Sahu BK, Fendzi Mbasso WF, Jangir P, Elrashidi A. Optimization-Based Energy Management for Grid-Connected Photovoltaic–Battery Systems in Smart Grids Using Demand Response and Particle Swarm Optimization. Engineering Reports 2025;7. https://doi.org/10.1002/eng2.70305.

Received on 2026-03-26 Accepted on 2026-05-07